FRONTIER LETTER

Open Access

Rupture process of the 2016 Kumamoto earthquake in relation to the thermal structure around Aso volcano

Yuji Yagi[1*], Ryo Okuwaki[2], Bogdan Enescu[3], Amato Kasahara[2], Ayumu Miyakawa[4] and Makoto Otsubo[4]

Abstract

We constructed the rupture process model for the 2016 Kumamoto, Japan, earthquake from broadband teleseismic body waveforms (P-waves) by using a novel waveform inversion method that takes into account the uncertainty of Green's function. The estimated source parameters are: seismic moment = 5.1×10^{19} Nm (Mw = 7.1), fault length = 40 km, and fault width = 15 km. The mainshock rupture mainly propagated northeastward from the epicenter, for about 30 km, along an active strike-slip fault. The rupture propagation of the mainshock decelerated and terminated near the southwest side of the Aso volcano; the aftershock activity was low around the northeastern edge of the major slip area. Our results suggest that the rupture process of the mainshock and the distribution of aftershocks were influenced by the high-temperature area around the magma chamber of Mt. Aso.

Keywords: 2016 Kumamoto earthquake, Rupture process, Foreshocks and aftershocks, Mt. Aso, Magma chamber

Introduction

A large and destructive earthquake (M_{JMA} 7.3) occurred on April 15, 2016 [Coordinated Universal Time (UTC)], in Kumamoto region, Kyushu Island, Japan. The origin time of the earthquake was April 16, 2016, 01:25 [Japan Standard Time (JST)], its epicenter was located at 32.76°N, 130.76°E, and its hypocentral depth was 12 km, as determined by the Japan Meteorological Agency (JMA). Figure 1a shows the largest foreshock (M_{JMA} 6.5) occurred on 14 April, the mainshock, and on- and off-fault aftershock activity within 3 days after the 2016 Kumamoto earthquake (epicenters determined by the JMA). The aftershock distribution and a focal mechanism determined in this study (Fig. 1a) indicate that the 2016 Kumamoto earthquake occurred along an active strike-slip fault, known as the Futagawa fault (Fig. 1a; Research Group for Active Faults of Japan 1991), which belongs to the Oita–Kumamoto Tectonic Line (OKTL; Fig. 1b) (e.g.,

Kamata and Kodama 1994) and is adjacent to the major shear zone in Kyushu (Matsumoto et al. 2015).

The geologic structure, which includes the Aso volcano, locates in the central part of the OKTL and might have contributed to the complex rupture process during foreshocks, mainshock, and aftershocks. The source model of the mainshock, in particular, may help to understand the seismicity evolution during the 2016 Kumamoto earthquake sequence in its geologic context. Here, we first determine the robust seismic source process of the 2016 Kumamoto earthquake by applying a novel inversion technique (Yagi and Fukahata 2011a) that takes into account the modeling errors due to the uncertainty of Green's function. Then, we discuss the relationship between the rupture process of the mainshock, seismicity, and the geologic structure around the Aso volcano. Understanding the relationship between seismicity and crustal geophysics (e.g., Hauksson 2011), in particular the crustal thermal structure (Enescu et al. 2009), may help in a better assessment of seismic hazard.
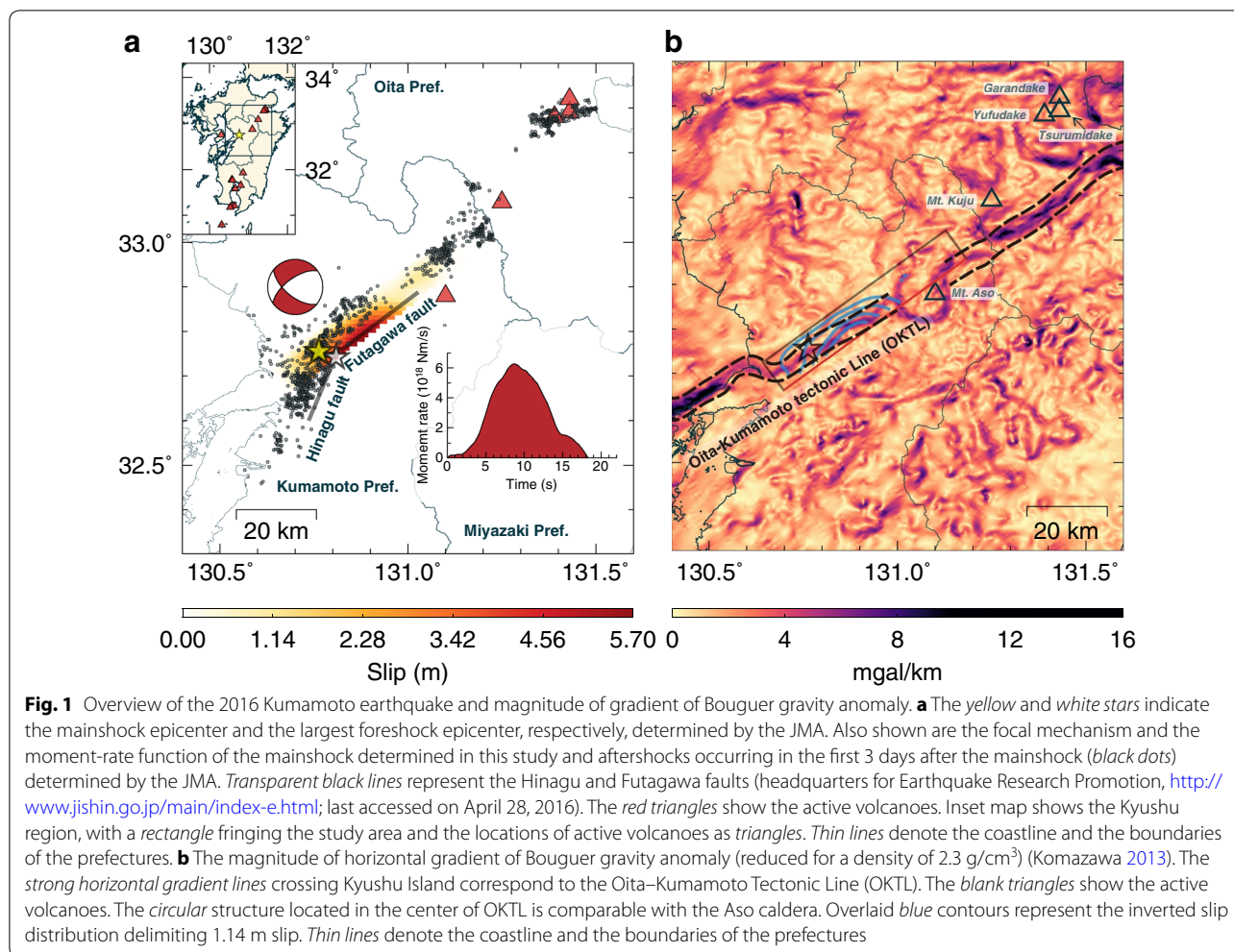
*Correspondence: yagi-y@geol.tsukuba.ac.jp
[1] Faculty of Life and Environmental Sciences, University of Tsukuba, 1-1-1 Ten'nodai, Tsukuba, Ibaraki 305-8572, Japan
Full list of author information is available at the end of the article

Methods

The spatiotemporal slip-rate distributions of large earthquakes have been estimated by waveform inversion since

Yagi *et al. Earth, Planets and Space* (2016) 68:118

Page 2 of 6

Fig. 1 Overview of the 2016 Kumamoto earthquake and magnitude of gradient of Bouguer gravity anomaly. **a** The *yellow* and *white stars* indicate the mainshock epicenter and the largest foreshock epicenter, respectively, determined by the JMA. Also shown are the focal mechanism and the moment-rate function of the mainshock determined in this study and aftershocks occurring in the first 3 days after the mainshock (*black dots*) determined by the JMA. *Transparent black lines* represent the Hinagu and Futagawa faults (headquarters for Earthquake Research Promotion, http://www.jishin.go.jp/main/index-e.html; last accessed on April 28, 2016). The *red triangles* show the active volcanoes. Inset map shows the Kyushu region, with a *rectangle* fringing the study area and the locations of active volcanoes as *triangles*. *Thin lines* denote the coastline and the boundaries of the prefectures. **b** The magnitude of horizontal gradient of Bouguer gravity anomaly (reduced for a density of 2.3 g/cm^3) (Komazawa 2013). The *strong horizontal gradient lines* crossing Kyushu Island correspond to the Oita–Kumamoto Tectonic Line (OKTL). The *blank triangles* show the active volcanoes. The *circular* structure located in the center of OKTL is comparable with the Aso caldera. Overlaid *blue* contours represent the inverted slip distribution delimiting 1.14 m slip. *Thin lines* denote the coastline and the boundaries of the prefectures
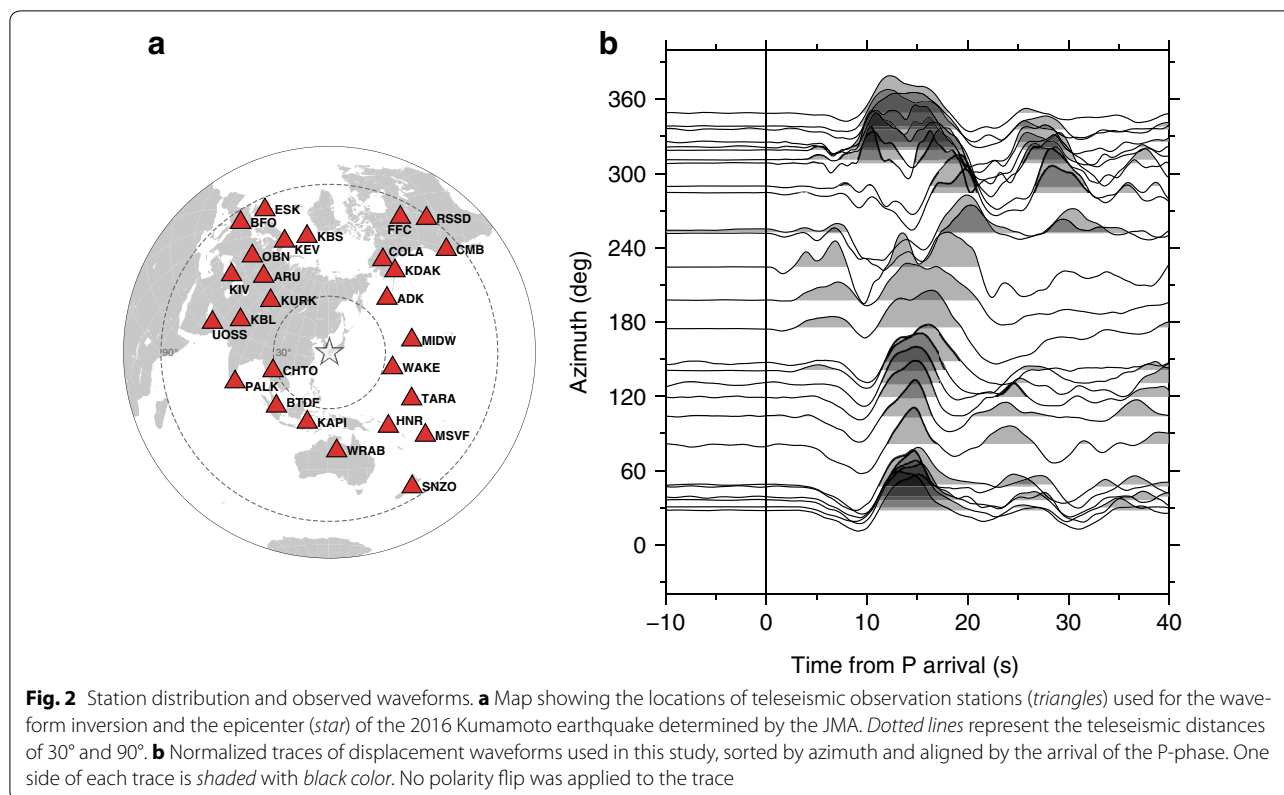
early 1980s (e.g., Hartzell and Heaton 1983). However, the results of inversions conducted for the same earthquake are often different from one another (e.g., Beresnev 2003). The modeling errors originated from the accuracy limitations of Green's function are a major problem in seismic source inversion studies and may often bias the inversion result.

To obtain a robust seismic source model for the 2016 Kumamoto earthquake, we applied the inversion formulation developed by Yagi and Fukahata (2011a) to teleseismic P-waves. This inversion formulation takes into account the uncertainty of Green's function and objectively determines the smoothness of the spatiotemporal slip-rate distribution from observed data, using the Akaike's Bayesian information criterion (e.g., Akaike 1980). Such features of the inversion formulation enable us to estimate the complex and irregular rupture process, including the back rupture propagation; the inversion formulation has been applied, for example, to the 2006 Java, Indonesia, tsunami earthquake (Yagi and Fukahata 2011a), the 2011 Tohoku-oki megathrust earthquake

(Yagi and Fukahata 2011b), the 2008 Wenchuan, China, earthquake (Yagi et al. 2012), and the 2015 Illapel, Chile, earthquake (Okuwaki et al. 2016). Yagi and Fukahata (2011a, b) show that if we neglect the data covariance components, the slip-rate distribution is distorted by modeling errors originated from the uncertainty of Green's function.

We have used the vertical component teleseismic P-wave data recorded at 27 broadband seismic stations (Fig. 2a). In general, we can obtain the robust slip-rate distribution of large earthquakes from teleseismic P-wave data, which are insensitive to the assumed structure (Yagi et al. 2004). We removed the seismograph response from the original waveforms to convert them into velocity waveforms and then re-sampled the waveform data at 0.3-s intervals. In order to mitigate aliasing and low frequency noise, a 0.001- to 0.56-Hz Butterworth band-pass filter was applied before re-sampling. The first arrival of P-phase on each original waveform was manually picked so that it corresponds to the initial rupture break.

Yagi *et al. Earth, Planets and Space* (2016) 68:118

Page 3 of 6

Fig. 2 Station distribution and observed waveforms. **a** Map showing the locations of teleseismic observation stations (*triangles*) used for the waveform inversion and the epicenter (*star*) of the 2016 Kumamoto earthquake determined by the JMA. *Dotted lines* represent the teleseismic distances of 30° and 90°. **b** Normalized traces of displacement waveforms used in this study, sorted by azimuth and aligned by the arrival of the P-phase. One side of each trace is *shaded* with *black color*. No polarity flip was applied to the trace

We assumed the rupture occurring on a single fault plane of (strike, dip) = (234°, 64°) and the fault area of 58 km length and 20 km width. The geographical coordinates of the initial break point are the same as for the JMA epicenter. The fault plane was slightly modified from that obtained by moment tensor inversion of teleseismic body waves to be consistent with the geometry and location of the Futagawa fault (Headquarters for Earthquake Research Promotion, http://www.jishin. go.jp/main/index-e.html; last accessed on April 28, 2016). For the same reason, the break point depth (i.e., hypocentral depth) was taken at 9 km. Assumed dip angle was shallower than the estimated value of the regional seismic network (National Research Institute for Earth Science and Disaster Resilience, Japan, http://www.fnet. bosai.go.jp/top.php?LANG=en; last accessed on June 13, 2016). We performed inversions using several dip angles and found that the center of the maximum slip area was stable (Additional file 1: Figure A2). We imposed no specific constraints on the rake angles. As the structure model near the source, we used CRUST 1.0 (Additional file 1: Table A1; Laske et al. 2013). We adopted a slip-rate function represented as linear B-splines with a grid interval of 0.3 s and having a duration of 15 s on each fault patch. The assumed rupture duration was taken as 18 s. The theoretical Green's functions of each source node were calculated with the method of Kikuchi and

Kanamori (1991). The maximum rupture front velocity, which defines the rupture onset time at each spatial node, was set to 2.4 km/s. The center of the maximum slip area was stable even when we have assumed various maximum rupture front velocities (Additional file 1: Figure A3). We also examined two kinds of initial slip model: uniform slip model and vertical striped slip models in the same way as Yagi and Fukahata (2011a), and found that exactly the same solution was obtained for both of the initial slip models.
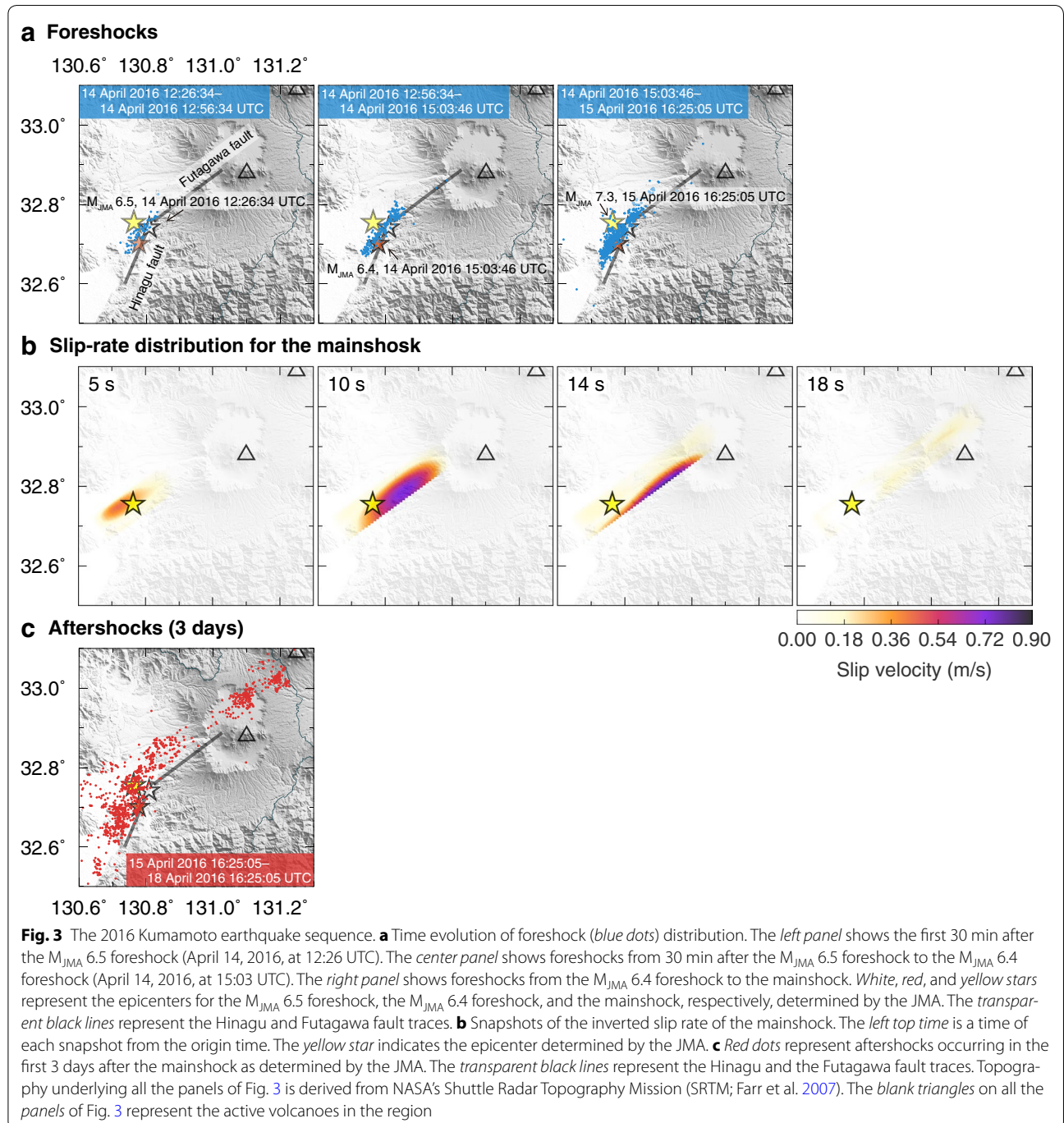
Results and discussion

The total slip distribution, the moment-rate function, and the focal mechanism are given in Fig. 1a. We found that the rupture mainly propagated toward northeast from the epicenter. The rupture direction is consistent with the characteristics of the mainshock waveforms (Fig. 2b), which are shorter toward northeast and broader toward southwest. The area of large slip, with a maximum of 5.7 m, is centered about 10 km northeast from the epicenter. The effective slip area extends about 40 km long and 15 km wide. The average rake angle was −148°, which is approximately consistent with the fault motion of historical earthquakes estimated by geological surveys (Research Group for Active Faults of Japan 1991). The total seismic moment was 5.1×10^{19} Nm (Mw = 7.0), which is comparable to the Global Centroid Moment

Yagi *et al. Earth, Planets and Space* (2016) 68:118

Page 4 of 6

Tensor solution of 4.5×10^{19} Nm (http://www.globalcmt.org; last accessed on April 28, 2016).

Figure 3 shows the distribution of foreshocks, the spatiotemporal slip rate of the mainshock, and the aftershocks. The foreshocks started in the northern part of an active strike-slip fault, known as the Hinagu fault (Fig. 3a), and expanded northeastward and southwestward along the Hinagu fault. The rupture of the mainshock started near the junction of the Hinagu and the Futagawa fault zones. Such a foreshock–mainshock rupture pattern is well known for complex fault zones (e.g., King and Nabelek 1985), suggesting that the foreshock activity near the junction between the Hinagu and Futagawa faults contributed to the initiation of the mainshock rupture.

The slip-rate distribution shows that the rupture propagated to southwest during the first 5 s. At 5 s after the origin time, the main rupture started to propagate toward

Fig. 3 The 2016 Kumamoto earthquake sequence. **a** Time evolution of foreshock (*blue dots*) distribution. The *left panel* shows the first 30 min after the M$_{JMA}$ 6.5 foreshock (April 14, 2016, at 12:26 UTC). The *center panel* shows foreshocks from 30 min after the M$_{JMA}$ 6.5 foreshock to the M$_{JMA}$ 6.4 foreshock (April 14, 2016, at 15:03 UTC). The *right panel* shows foreshocks from the M$_{JMA}$ 6.4 foreshock to the mainshock. *White*, *red*, and *yellow stars* represent the epicenters for the M$_{JMA}$ 6.5 foreshock, the M$_{JMA}$ 6.4 foreshock, and the mainshock, respectively, determined by the JMA. The *transparent black lines* represent the Hinagu and Futagawa fault traces. **b** Snapshots of the inverted slip rate of the mainshock. The *left top time* is a time of each snapshot from the origin time. The *yellow star* indicates the epicenter determined by the JMA. **c** *Red dots* represent aftershocks occurring in the first 3 days after the mainshock as determined by the JMA. The *transparent black lines* represent the Hinagu and the Futagawa fault traces. Topography underlying all the panels of Fig. 3 is derived from NASA's Shuttle Radar Topography Mission (SRTM; Farr et al. 2007). The *blank triangles* on all the *panels* of Fig. 3 represent the active volcanoes in the region

Yagi *et al. Earth, Planets and Space* (2016) 68:118

Page 5 of 6

northeast. The slip rate started decreasing from 15 s and terminated at about 17 s after the initial break. The on-fault aftershocks occurred along the Futagawa fault zone, and the off-fault aftershocks were triggered along the OKTL (Figs. 1a, 3c).

To better understand the complex relationship between the geologic structure, the rupture process of the mainshock, and the aftershock activity, we compare in Fig. 4 the land elevation (Fig. 4a), aftershock density (Fig. 4b), and shear stress change along the fault strike (Fig. 4c). We calculated the shear stress change corresponding to the average slip direction on the assumed fault plane using the formulation for a static dislocation in a homogeneous half-space (Okada 1992). The maximum stress drop was 9.5 MPa (Fig. 4c) near the largest slip area (Fig. 1a). On the other hand, we notice a zone of stress increase (stress rise values up to 5.6 MPa) immediately northeast of the large stress drop zone. The aftershock activity (Fig. 4b) is highest in the hypocentral region [Fig. 4b: (−5 to +10 km), along strike], next to the area of large stress drop during the mainshock. Note that the enhanced aftershock activity here is likely the result of "superposed" aftershocks of the mainshock and largest (M_{JMA} 6.5) foreshock (Fig. 3a, c). The along-strike aftershock density decreases gradually toward northeast [0 to −20 km, along strike]. The moderate aftershock activity taking place at the same along-strike distances [Fig. 4b: (−5 to −15 km), along strike] as the maximum shear stress drop reflects mainly deeper aftershock activity (i.e., below the large slip area, see Figs. 1a, 4c). Further to the northeast, there is a quite sudden decrease in the aftershock activity toward very low levels [Fig. 4b: (−20 to −30 km), along strike], followed by an along-strike increase that reaches a maximum [Fig. 4b: ~(−40 km), along strike] around the northeastern edge of the Aso volcano. Note that it is difficult to discuss the relationship between this northeastern-most increase in seismicity and the shear stress change due to small slip near the northeastern edge (Figs. 1a, 4c), since the uncertainty of slip distribution increases with distance from the hypocenter (Yagi and Fukahata 2011a). However, it is clear that the aftershock activity is low around the rupture deceleration area, where the shear stress was increasing due to the coseismic slip of the mainshock, and thus, we would have expected an increased aftershock activity. In general, high-temperature areas promote plastic deformation and inhibit dynamic rupture propagation during earthquakes (e.g., Scholz 1998). A tomography study conducted in the region shows that the low seismic velocity sphere, located shallower than 10 km beneath the Aso volcano, relates to the existence of a magma chamber (Sudo and Kong 2001). The thermal structure model determined by magnetic data (Okubo and Shibuya 1993) shows that the
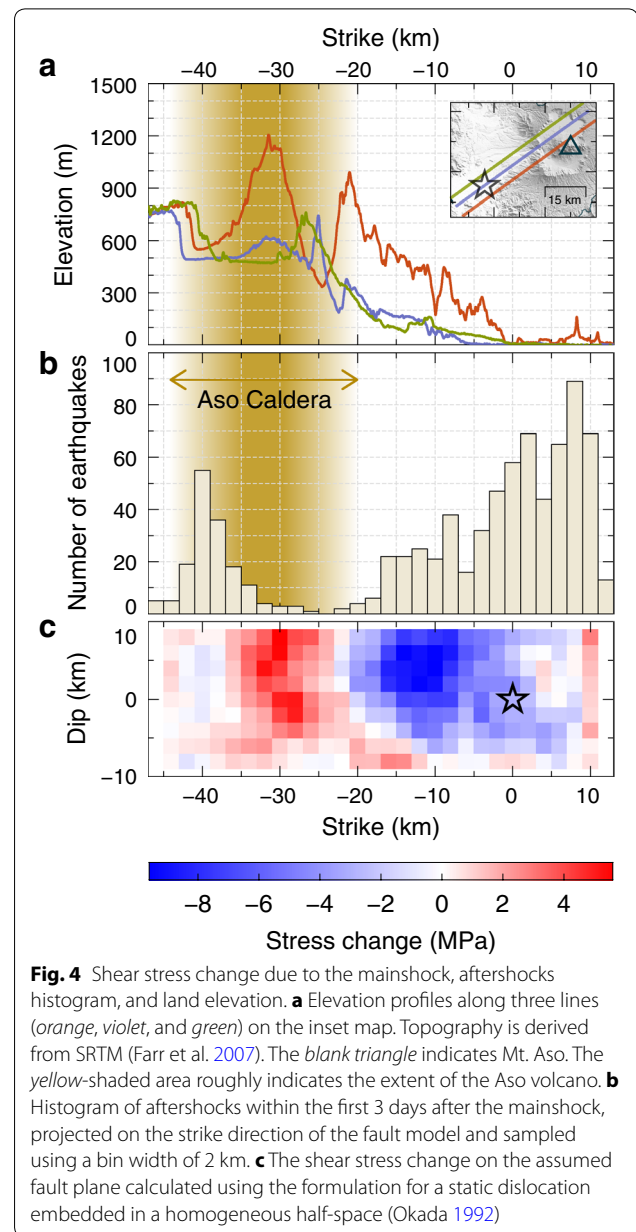

Fig. 4 Shear stress change due to the mainshock, aftershocks histogram, and land elevation. **a** Elevation profiles along three lines (*orange*, *violet*, and *green*) on the inset map. Topography is derived from SRTM (Farr et al. 2007). The *blank triangle* indicates Mt. Aso. The *yellow*-shaded area roughly indicates the extent of the Aso volcano. **b** Histogram of aftershocks within the first 3 days after the mainshock, projected on the strike direction of the fault model and sampled using a bin width of 2 km. **c** The shear stress change on the assumed fault plane calculated using the formulation for a static dislocation embedded in a homogeneous half-space (Okada 1992)

high temperature (over approximately 500 °C) reached to about 3 km beneath the Aso caldera. The high-temperature area around the magma chamber of Mt. Aso may have contributed to the termination of the rupture during the mainshock and the low aftershock activity around the Aso volcano.

Conclusions

We estimated the robust spatiotemporal slip-rate distribution of the 2016 Kumamoto earthquake using the waveform inversion of teleseismic P-wave data and examined the 2016 Kumamoto earthquake sequence, including the foreshock and aftershock activity. The foreshocks started

Yagi *et al. Earth, Planets and Space* (2016) 68:118

Page 6 of 6

in the northern part of the Hinagu fault, and the rupture of the mainshock initiated at the junction between the Hinagu and the Futagawa fault zones. The dynamic rupture of the mainshock mainly propagated 30 km northeastward from the epicenter, along the Futagawa fault. The rupture of the mainshock decelerated and terminated near the southwest side of the Aso volcano, and aftershock activity was low around the northeastern edge of the major slip area (where shear stress was increasing due to the coseismic slip of the mainshock). The high-temperature area around the magma chamber of Mt. Aso may contribute to the termination of the rupture during the mainshock and peculiarly low aftershock activity of the 2016 Kumamoto earthquake, around Mt. Aso.

Additional file

Additional file 1: Figure A1. Waveform fittings between observed and synthetic waveforms. **Figure A2.** Alternative slip models calculated based on various assumptions of dip angle. **Figure A3.** Alternative slip models calculated based on various maximum rupture velocities. **Table A1.** 1-D structural velocity model of the near the source region used for calculating Green's functions.

Authors' contributions
YY led and designed the whole research and drafted the manuscript. RO carried out the inversion analysis, generated the figures and Additional file, and contributed to the examination of the results. BE and AK contributed to the discussion of the results. AM contributed to generate the contents of Fig. 1b. AM and MO contributed to the interpretation of the results related to the local and regional geology. All authors discussed the results and commented on the manuscript. All authors read and approved the final manuscript.

Author details
[1] Faculty of Life and Environmental Sciences, University of Tsukuba, 1-1-1 Ten'nodai, Tsukuba, Ibaraki 305-8572, Japan. [2] Graduate School of Life and Environmental Sciences, University of Tsukuba, 1-1-1 Ten'nodai, Tsukuba, Ibaraki 305-8572, Japan. [3] Department of Geophysics, Faculty of Science, Kyoto University, Kita-Shirakawa Oiwake-cho, Sakyo-ku, Kyoto 606-8502, Japan. [4] Geological Survey of Japan, AIST, 1-1-1 Higashi, Tsukuba, Ibaraki 305-8568, Japan.

Competing interests
The authors declare that they have no competing interests.

References
Akaike H (1980) Likelihood and the Bayes procedure. In: Bernardo JM, DeGroot MH, Lindley DV, Smith AFM (eds) Bayesian Statistics. University Press, Valencia, pp 143–166

Beresnev IA (2003) Uncertainties in finite-fault slip inversions: to what extent to believe? (a critical review). Bull Seismol Soc Am 93:2445–2458. doi:10.1785/0120020225

Enescu B, Hainzl S, Ben-Zion Y (2009) Correlations of seismicity patterns in Southern California with surface heat flow data. Bull Seismol Soc Am 99(6):3114–3123. doi:10.1785/0120080038

Farr TG, Rosen PA, Caro E, Crippen R, Duren R, Hensley S, Kobrick M, Paller M, Rodriguez E, Roth L, Seal D, Shaffer S, Shimada J, Umland J, Werner M, Oskin M, Burbank D, Alsdorf D (2007) The shuttle radar topography mission. Rev Geophys 45:RG2004. doi:10.1029/2005RG000183

Hartzell S, Heaton T (1983) Inversion of strong ground motion and teleseismic waveform data for the fault rupture history of the 1979 Imperial Valley, California, earthquake. Bull Seismol Soc Am 73:1553–1583

Hauksson E (2011) Crustal geophysics and seismicity in southern California. Geophys J Int 186:82–98. doi:10.1111/j.1365-246X.2011.05042.x

Kamata H, Kodama K (1994) Tectonics of an arc-arc junction: an example from Kyushu Island at the junction of the Southwest Japan Arc and the Ryukyu Arc. Tectonophysics 233:69–81

Kikuchi M, Kanamori H (1991) Inversion of complex body waves—III. Bull Seismol Soc Am 81:2335–2350

King G, Nabelek J (1985) The role of fault bends in the initiation and termination of earthquake rupture. Science 228:984–987

Komazawa M (2013) Gravity grid data of Japan. In: Survey Geological, Geological Survey of Japan (eds) Gravity database of Japan DVD edition Digital Geoscience Map P-2. Geological Survey of Japan, AIST, Tsukuba

Laske G, Masters G, Ma Z, Pasyanos M (2013) Update on CRUST1.0—A 1-degree Global Model of Earth's Crust. Geophys Res Abstracts 15:EGU2013-2658

Matsumoto S, Nakao S, Ohkura T, Miyazaki M, Shimizu H, Abe Y (2015) Spatial heterogeneities in tectonic stress in Kyushu, Japan and their relation to a major shear zone. Earth Planets Space, Japan. doi:10.1186/s40623-015-0342-8

Okada Y (1992) Internal deformation due to shear and tensile faults in a half-space. Bull Seism Soc Am 82:1018–1040

Okubo Y, Shibuya A (1993) Thermal and crustal structure of the Aso volcano and surrounding regions constrained by gravity and magnetic data, Japan. J Volcanol Geotherm Res 55:337–350

Okuwaki R, Yagi Y, Aránguiz R, González J, González G (2016) Rupture process during the 2015 Illapel, Chile earthquake: zigzag-along-dip rupture episodes. Pure appl Geophys 173:1011–1020. doi:10.1007/s00024-016-1271-6

Research group for active faults of Japan (1991) Active faults in Japan. Sheet maps and inventories, Revised Edition. University of Tokyo Press, Tokyo

Scholz CH (1998) Earthquake and friction laws. Nature 391:37–42. doi:10.1038/34097

Sudo Y, Kong L (2001) Three-dimensional seismic velocity structure beneath Aso Volcano, Kyushu, Japan. Bull Volcanol 63:326–344. doi:10.1007/s004450100145

Wessel P, Smith WHF (1998) New, improved version of generic mapping tools released. EOS Trans Am Geophys Union 79:579. doi:10.1029/98EO00426

Yagi Y, Fukahata Y (2011a) Introduction of uncertainty of Green's function into waveform inversion for seismic source processes. Geophys J Int 186:711–720. doi:10.1111/j.1365-246X.2011.05043.x

Yagi Y, Fukahata Y (2011b) Rupture process of the 2011 Tohoku-oki earthquake and absolute elastic strain release. Geophys Res Lett 38:1–6. doi:10.1029/2011GL048701

Yagi Y, Mikumo T, Pacheco J, Reyes G (2004) Source rupture process of the Tecoman, Colima, Mexico earthquake of January 22, 2003, determined by joint inversion of teleseismic body wave and near source data. Bull Seism Soc Am 94:1795–1807

Yagi Y, Naoki N, Kasahara A (2012) Source process of the 12 May 2008 Wenchuan, China, earthquake determined by waveform inversion of teleseismic body waves with a data covariance matrix. Earth Planets Space 64:e13–e16. doi:10.5047/eps.2012.05.006